

---

---

# Kinetic Analysis of 3'-Deoxy-3'-<sup>18</sup>F-Fluorothymidine in Patients with Gliomas

Mark Muzi<sup>1</sup>, Alexander M. Spence<sup>2</sup>, Finbarr O'Sullivan<sup>3</sup>, David A. Mankoff<sup>1</sup>, Joanne M. Wells<sup>1</sup>, John R. Grierson<sup>1</sup>, Jeanne M. Link<sup>1</sup>, and Kenneth A. Krohn<sup>1</sup>

<sup>1</sup>Department of Radiology, University of Washington, Seattle, Washington; <sup>2</sup>Department of Neurology, University of Washington, Seattle, Washington; and <sup>3</sup>Department of Statistics, University College Cork, Cork, Ireland

3'-Deoxy-3'-fluorothymidine (FLT), a thymidine analog, is under investigation for monitoring cellular proliferation in gliomas, a potential measure of disease progression and response to therapy. Uptake may result from retention in the biosynthetic pathway or leakage via the disrupted blood-tumor barrier. Visual analysis or static measures of <sup>18</sup>F-FLT uptake are problematic as transport and retention cannot be distinguished. **Methods:** Twelve patients with primary brain tumors were imaged for 90 min of dynamic <sup>18</sup>F-FLT PET with arterial blood sampling. Total blood activity was corrected for labeled metabolites to provide an FLT input function. A 2-tissue compartment, 4-rate-constant model was used to determine blood-to-tissue transport ( $K_1$ ) and metabolic flux ( $K_{FLT}$ ). Modeling results were compared with MR images of blood-brain barrier (BBB) breakdown revealed by gadolinium (Gd) contrast enhancement. Parametric image maps of  $K_1$  and  $K_{FLT}$  were produced by a mixture analysis approach. **Results:** Similar to prior work with <sup>11</sup>C-thymidine, identifiability analysis showed that  $K_1$  (transport) and  $K_{FLT}$  (flux) could be estimated independently for sufficiently high  $K_1$  values. However, estimation of  $K_{FLT}$  was less robust at low  $K_1$  values, particularly those close to normal brain.  $K_1$  was higher for MRI contrast-enhancing (CE) tumors ( $0.053 \pm 0.029$  mL/g/min) than noncontrast-enhancing (NCE) tumors ( $0.005 \pm 0.002$  mL/g/min;  $P < 0.02$ ), and  $K_{FLT}$  was higher for high-grade tumors ( $0.018 \pm 0.008$  mL/g/min,  $n = 9$ ) than low-grade tumors ( $0.003 \pm 0.003$  mL/g/min,  $n = 3$ ;  $P < 0.01$ ). The flux in NCE tumors was indistinguishable from contralateral normal brain ( $0.002 \pm 0.001$  mL/g/min). For CE tumors,  $K_1$  was higher than  $K_{FLT}$ . Parametric images matched region-of-interest estimates of transport and flux. However, no patient has <sup>18</sup>F-FLT uptake outside of the volume of increased permeability defined by MRI T1+Gd enhancement. **Conclusion:** Modeling analysis of <sup>18</sup>F-FLT PET data yielded robust estimates of  $K_1$  and  $K_{FLT}$  for enhancing tumors with sufficiently high  $K_1$  and provides a clearer understanding of the relationship between transport and retention of <sup>18</sup>F-FLT in gliomas. In tumors that show breakdown of the BBB, transport dominates <sup>18</sup>F-FLT uptake. Transport across the BBB and modest rates of <sup>18</sup>F-FLT phosphorylation appear to limit the assessment of cellular proliferation using <sup>18</sup>F-FLT to highly proliferative tumors with significant BBB breakdown.

**Key Words:** 3'-deoxy-3'-fluorothymidine; kinetic modeling; glioma; blood-brain barrier disruption; thymidine kinase 1

**J Nucl Med 2006; 47:1612-1621**

**P**ET of cellular proliferation may provide a convenient and early measure of therapeutic response in cancer patients (1-4). Radiolabeled thymidine (2-<sup>11</sup>C-thymidine [TdR]) is the most direct indicator of proliferation by PET (5,6). It is rapidly incorporated into DNA through the exogenous (salvage) pathway for pyrimidines. Quantitative estimates of TdR uptake in tumors treated with chemotherapy exhibit larger and more consistent decreases after therapy compared with decreases in FDG (3). However, static imaging of TdR does not accurately reflect proliferation because labeled metabolites, especially <sup>11</sup>C-CO<sub>2</sub> in the brain, contaminate the images (6). Accurate interpretation of TdR uptake to determine the rate of DNA synthesis requires rapid arterial sampling, extensive plasma metabolite analysis, and mathematic modeling of the PET data. This is particularly true of brain tumors, where the normal blood-brain barrier (BBB) limits TdR transport (1,4,7).

Recently, 3'-deoxy-3'-<sup>18</sup>F-fluorothymidine (FLT), a TdR analog, has been developed as an alternative to TdR for imaging proliferation (5,8). <sup>18</sup>F-FLT offers the advantages of a longer-lived label with high specificity for thymidine kinase 1 (TK1) in the cytosol and few labeled metabolites. TK1 is highly regulated during the cell cycle and is highly expressed during S phase. Further FLT tissue metabolism produces phosphorylated products (nucleotides), which are retained in cells at a rate proportional to TK1 activity (9). FLT is not significantly incorporated into DNA because it lacks the 3'-hydroxyl, which is essential for chain propagation. <sup>18</sup>F-FLT labels the intracellular nucleotide pool and is subject to retrograde metabolism (9). FLT anabolism primarily occurs in the liver to produce a glucuronide conjugate, which is exported to the blood and cleared by the kidneys (10). <sup>18</sup>F-FLT-glucuronide appears to be the only observed metabolite contaminating the blood pool (10).

---

Received May 11, 2006; revision accepted Jul. 25, 2006.  
For correspondence or reprints contact: Mark Muzi, MS, University of Washington-Radiology, Box 356004, 1959 N.E. Pacific St., Seattle, WA 98195-6004.  
E-mail: muzi@u.washington.edu  
COPYRIGHT © 2006 by the Society of Nuclear Medicine, Inc.

We have previously described a 2-tissue compartment, 4-rate constant model (2C) for  $^{18}\text{F}$ -FLT that has been validated for somatic tissues and successfully applied to patient studies (11,12). However, because the intact BBB restricts the transport of modified pyrimidine nucleotides such as FLT (7,13), and tumor growth or therapy can disrupt the BBB (14), further analysis was necessary to demonstrate that the model could distinguish between increased transport across a damaged BBB and increased retention of  $^{18}\text{F}$ -FLT in proliferating tumor tissue.

## MATERIALS AND METHODS

### Patients

All tumors were graded by the World Health Organization (WHO) scheme. Twelve patients were included in the analysis (8 male, 4 female; mean age, 47 y; range, 19–67 y): 4 with glioblastoma multiforme (WHO grade IV), 1 with gliosarcoma (WHO grade IV), 1 with anaplastic pleomorphic xanthoastrocytoma (WHO grade III), 2 with anaplastic astrocytoma (WHO grade III), 1 with oligodendroglioma (WHO grade III), and 3 with oligodendroglioma (WHO grade II) listed in Table 1. Histopathology was performed on tissue specimens recovered at biopsy ( $n = 5$ ) or resection ( $n = 7$ ) before  $^{18}\text{F}$ -FLT PET. All patients had contrast-enhanced (CE) MRI within 30 d of PET. Six patients had prior radiation and chemotherapy, whereas 4 received prior radiotherapy only, 1 had prior chemotherapy only, and 1 had no treatment before PET. These protocols were approved by the University of Washington Human Subjects and Radiation Safety committees and the Radioactive Drug Research Committee. Patients were tested for hemotologic, renal, and liver function before and after PET and provided signed informed consent.

### Radiosynthesis

FLT was prepared by the method of either Grierson et al. (8) or Blocher et al. (15). The specific activity was  $>7.4$  GBq/ $\mu\text{mol}$  at injection, and the radiochemical purity was  $>98\%$ . Before release and administration of each dose, quality tests for endotoxins, pH, and chemical or radiochemical purity were completed. U.S.

Pharmacopeia (USP) sterility testing was performed on samples of each batch.  $^{18}\text{F}$ -FLT was administered by intravenous injection of a 10-mL solution of isotonic saline containing  $<10\%$  (v/v) ethanol USP. The injected dose was based on the patient's weight (2.59 MBq/kg), with a 185-MBq maximum, an amount that is as low as reasonably achievable and still permits the acquisition of dynamic images for kinetic analysis.

### Imaging Procedure

The PET studies were performed on an Advance PET tomograph (GE Healthcare) providing 35 image planes over a 15-cm axial field of view with a 4.25-mm spacing (16). While a 25-min transmission scan with a  $^{68}\text{Ge}$  rotating sector source was underway, intravenous and intraarterial lines were introduced for isotope injection and arterial sampling. Arterial samples of 1 mL were obtained using an automated blood sampler (17) at  $8 \times 15$  s,  $2 \times 30$  s,  $5 \times 1$  min,  $1 \times 2$  min, and  $16 \times 5$  min. Images were acquired in 3-dimensional (3D) mode with a dynamic sequence:  $10 \times 10$  s,  $4 \times 20$  s,  $3 \times 40$  s,  $3 \times 1$  min,  $5 \times 2$  min,  $4 \times 3$  min, and  $12 \times 5$  min time frames for a total of 90 min. After correction for scattered and random coincidences, images were reconstructed by the method of 3D reprojection (18) with 6-mm Hanning, 4.5-mm radial, and 6-mm smoothing filters, resulting in an approximately isotropic image resolution of 6 mm.

### Blood Sampling and Metabolite Analysis

For each arterial blood sample, 0.2 mL plasma were assayed for radioactivity using a COBRA  $\gamma$ -counter (Packard Instruments). Because FLT has negligible serum protein binding (19), all of the activity associated with  $^{18}\text{F}$ -FLT in blood was assumed to be available for tissue uptake. An aliquot (0.4 mL) of the plasma from 8 arterial samples (5, 10, 15, 20, 30, 45, 60, and 90 min) was assayed for the relative amount of FLT and FLT-glucuronide as described previously (11,20). The fraction of total activity present as FLT in each blood sample was fitted to a monoexponential curve to provide a continuous function describing the fraction of plasma activity associated with FLT (11). The fractional FLT curve was applied to each total blood activity curve to give a

TABLE 1  
Patient Clinical Data

Patient no.	Sex	Age (y)	Histology	WHO grade	Therapy before PET			MRI CE
					Dx	RT (Gy)	Ch	
1	M	67	Gliosarcoma	IV	Sx	63		Yes
2	M	61	Astrocytoma	III	Bx	59		No
3	M	44	Oligodendroglioma	II	Bx			No
4	F	44	Astrocytoma	III	Bx	59		Yes
5	M	45	Glioblastoma multiforme	IV	Sx	59	Yes	Yes
6	M	56	Oligodendroglioma	II	Sx		Yes	No
7	M	60	Glioblastoma multiforme	IV	Sx	59	Yes	Yes
8	F	24	Xanthoastrocytoma	III	Bx	54	Yes	Yes
9	F	41	Glioblastoma multiforme	IV	Sx	59	Yes	Yes
10	F	19	Oligodendroglioma	III	Sx	59		Yes
11	M	46	Oligodendroglioma	II	Bx	54	Yes	Yes
12	M	62	Glioblastoma multiforme	IV	Sx	59	Yes	Yes

Dx = diagnosis method; RT = radiotherapy; Gy = RT dose in gray; Ch = chemotherapy; MRI CE = contrast enhancement with MRI T1+Gd; Sx = surgery; Bx = biopsy.

metabolite-corrected input function for further modeling analysis of each patient dataset.

### Image Processing

MRI was performed with a 1.5-T Signa (GE Healthcare) with a standard head coil. The protocol for all subjects included a T1-weighted sequence acquired in the transverse plane before and after administration of intravenous gadolinium (Gd). MR images were coregistered to summed PET images with a method based on mutual information criteria (11).

Regions of interest (ROIs) for tumor and contralateral (C/L) brain regions (brain, gray and white matter) were identified on MRI T1+Gd or T2-weighted images and  $^{18}\text{F}$ -FLT images summed between 30 and 60 min, an interval when transport of the radiotracer from blood to tissue is predominantly unidirectional. The ROIs from contiguous slices were combined to create volumes of interest (VOIs) for each tissue type by means of Alice image-processing software (Perceptive Informatics, Inc.). Tumor regions were placed on all planes containing portions of the lesion as indicated from the MRI T1+Gd or  $^{18}\text{F}$ -FLT images.

### Quantitative Analysis

**Compartmental Modeling.** The previously described 2C kinetic model for FLT kinetics is illustrated in Figure 1 (12). Similar to the kinetic assumptions of the TdR model in brain tumors (21), FLT transport into the brain is influenced by blood flow and the BBB (13). Details of the FLT model have been reported previously (12).

The transfer from blood into tissue across the BBB is represented by  $K_1$ , whereas the return of FLT from tissue representing nonphosphorylated FLT back to blood is represented by  $k_2$ . The metabolic trapping of FLT through phosphorylation is represented by  $k_3$  and is the rate-limiting step for the intracellular trapping of FLT in tissue (12). Unlike TdR, which can be trapped irreversibly in DNA, there is some evidence that nucleotides of FLT can leave the imaging region either by dephosphorylation and subsequent efflux or via nucleotide transporters (9,22). The loss of image signal through these processes is described by  $k_4$  (12).

Metabolic flux,  $K_{FLT}$ , is estimated from parameters derived by fitting the FLT input function and the total blood activity curve to the tissue time-activity curve data. The flux constant is determined by the product of the rate constants (12,23):

$$K_{FLT} = \frac{K_1 k_3}{k_2 + k_3} = \frac{K_1 k_3}{(K_1/V_d) + k_3}, \quad \text{Eq. 1}$$

where  $V_d$  is the early distribution volume for the reversible compartment, given by  $K_1/k_2$ , similar to prior reports (12,21). The key parameters for describing  $^{18}\text{F}$ -FLT uptake in tissue are the blood-tissue transport rate,  $K_1$ , and the metabolic flux constant,  $K_{FLT}$ .

**Model Starting Parameters.** In our previous FLT tissue model (11), early analyses suggested that it was difficult to estimate  $K_1$  and  $k_2$  independently. Hence, the model was reparameterized using  $K_1$  and  $K_1/k_2$  as floating variables, which has been an effective method for handling  $K_1$ - $k_2$  covariance (6,12,21). The individual rate constants,  $K_1$ ,  $K_1/k_2$ ,  $k_3$ , and  $k_4$ , and the regional  $V_b$ , the fraction of vascular activity in the tissue VOI, were estimated during parameter optimization.

Starting parameters for FLT were based on FLT kinetic assessment of lung tumors (11) and TdR in gliomas (4). Prior studies in somatic tumors (11) have shown that estimates of the transport rate for FLT are lower than those for TdR (6). A lower  $K_1$  for FLT relative to TdR is expected, as cellular TdR transporters do not effectively transport analogs modified at the 3' position (24,25). Phosphorylation of FLT by TK1 ( $k_3$ ) is also anticipated to be lower than that for TdR, reflecting the differences in activity of TK1 for each substrate (26,27). Dephosphorylation of FLT-monophosphate, represented by  $k_4$  as estimated in lung tumors and muscle (11), is anticipated to occur at a similar level for gliomas and brain tissue. Thus, the initial model conditions were adjusted from the TdR starting points to reflect the less reactive behavior of FLT (Table 2).

For each time frame of the dynamic imaging sequence, the average Bq/mL within the VOI was used for compartmental analysis in the 2C model (Fig. 1). The regional VOI activity curves, the metabolite-corrected arterial input curve, and the total arterial activity curve were fitted to the FLT compartmental model using the weighted Levenberg-Marquart least-squares minimization algorithm as implemented in a software package designed for PET data analysis (PMOD version 2.65; PMOD group, Zurich, Switzerland). In the optimization process, the residuals were weighted by the inverse variance of the total counting rate in each frame of data, based on the SD of the total uncorrected counts and the duration of the time frame (28). Model parameters were estimated by minimizing the weighted residual sum of the square error (WRRS) between the model solution and the PET measurement.

**Model Characteristics.** The proposed model was evaluated to determine the extent to which the information obtained from a typical imaging study is sufficient to produce a unique solution with identifiable parameters. To establish the most reliable approach for parameter estimation, the brain FLT model was characterized with respect to (a) parameter sensitivity, the degree to which a change in an individual input parameter results in a change in the output; (b) parameter identifiability, the ability of the model to estimate parameters independently; (c) susceptibility to noise, as determined by Monte Carlo error analysis; and (d) model accuracy, the ability to estimate key parameters accurately across the expected range of values. These methods have been described (6,12,21) and are not repeated here.

**Parametric Image Analysis.** Parametric image maps of each rate constant were generated by mixture analysis (28,29). Mixture analysis applies the same biologically based model with identical

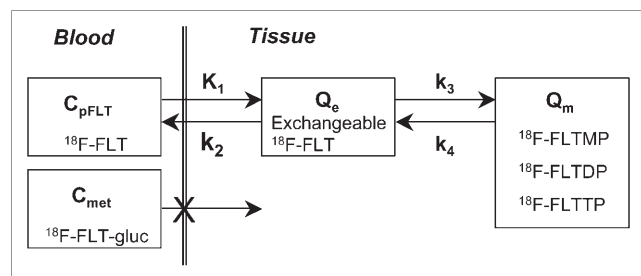


**FIGURE 1.** Kinetic model of FLT metabolism is comprised of an exchangeable tissue compartment ( $Q_e$ ) and a compartment of trapped FLT nucleotides ( $Q_m$ ). Four rate constants ( $K_1$ - $k_4$ ) describe kinetic transfer rates between the 2 compartments and blood. FLTMP = FLT-monophosphate; FLTDp = FLT-diphosphate; FLTTp = FLT-triphosphate; FLT-gluc = FLT-glucuronide;  $C_{pFLT}$  = concentration of FLT in arterial plasma;  $C_{met}$  = concentration of metabolites in arterial plasma.

**TABLE 2**  
FLT Model Parameters, Expected Ranges, and Starting Values

Parameter (units)	Function	TdR in glioma*	FLT in lung CA†	Starting value	Optimization range
$K_1$ (mL/min/g)	FLT transport	0.057	0.153	0.05	0.001, 0.5
$K_1/k_2$ (mL/g)	Tissue FLT volume	0.512	0.854	0.5	0.01, 1.0
$k_3$ (min <sup>-1</sup> )	FLT phosphorylation	0.106	0.242	0.1	0.001, 1.0
$k_4$ (min <sup>-1</sup> )	FLT-MP dephosphorylation	—	0.018	0.01	0.001, 0.1
$V_b$ (mL/g)	Vascular volume	0.036	0.073	0.05	0.01, 0.1

\*Data from Wells et al. (4) for  $n = 6$  CE brain tumors.

†Data from Muzi et al. (11) for  $n = 18$  lung cancers.

floating parameters and blood input functions used in the analysis of tissue time–activity curves to the dynamic series of images for the production of regional parametric maps. The VOIs used to generate tissue time–activity curves were applied to the parametric images to determine the extent of FLT flux relative to Gd enhancement on MR images, as well as the precision and bias of the parametric image values relative to modeling analysis of tissue time–activity curves.

**Model-Independent Analysis.** Simple, model-independent estimates of <sup>18</sup>F-FLT uptake were assessed by the standard uptake value (SUV) determined from images obtained between 30 and 60 min after injection and by a modified graphical analysis (GA) (30), which corrects for blood metabolites. The GA determination of flux may be valid for a short interval after injection, when the assumption of unidirectional transfer of FLT from blood to tissue is applicable (31). Because of the restricted transport of FLT, tissue pools of precursor require a greater time to stabilize with respect to blood delivery. Therefore, 30 and 60 min were chosen as the time boundaries for the linear fit in GA after examination of linearity in CE brain tumor regions. This is a different time range than that determined for lung tumors (15–50 min), where initial transport of FLT into lung tumors is greater (11). The method also assumes that phosphorylated FLT nucleotides are completely retained in the tissue, an assumption that has yet to be validated in vivo and is not supported by cell culture experiments (9).

### Statistical Analysis

The comparisons between <sup>18</sup>F-FLT PET uptake parameters or model estimations were made using standard parametric statistical tests (Pearson correlation, paired Student *t* test). Statistical analyses were performed using the statistical software JMP (SAS Institute).

## RESULTS

### Blood Activity Curves

Arterial FLT blood activity curves were similar in magnitude and profile to those observed in lung cancer patients (11,20). The proportion of total blood activity associated with FLT showed an average of 73% at 90 min (range, 93%–61%;  $n = 12$  patients).

### Sensitivity Analysis

Parameter sensitivity for other brain regions (gray and white matter) and noncontrast-enhancing (NCE) tumors were similar to C/L brain. In CE tumors,  $K_1$  has a greater contribution to <sup>18</sup>F-FLT uptake than phosphorylation,  $k_3$ .

The sensitivity of  $K_1$  for CE tumor is similar to TdR in magnitude and time course (21), with a large impact on early model output that diminishes after 10 min. The  $k_3$  phosphorylation rate had the greatest sensitivity of any individual rate constant during the prolonged <sup>18</sup>F-FLT uptake phase after blood–tissue equilibration (Fig. 2).

### Correlation Matrix

Identifiability analysis of glioma time–activity curves showed that individual parameters covaried, but  $K_1$  is quite robust and estimated independently (Table 3). There was a high level of covariance between  $k_3$  and  $V_d$  for CE gliomas, indicating it is difficult to obtain independent estimates of  $k_3$  and  $V_d$ .

### Monte Carlo Error

The results for 250 simulations on the effect of noise on parameter estimation using the Monte Carlo approach for

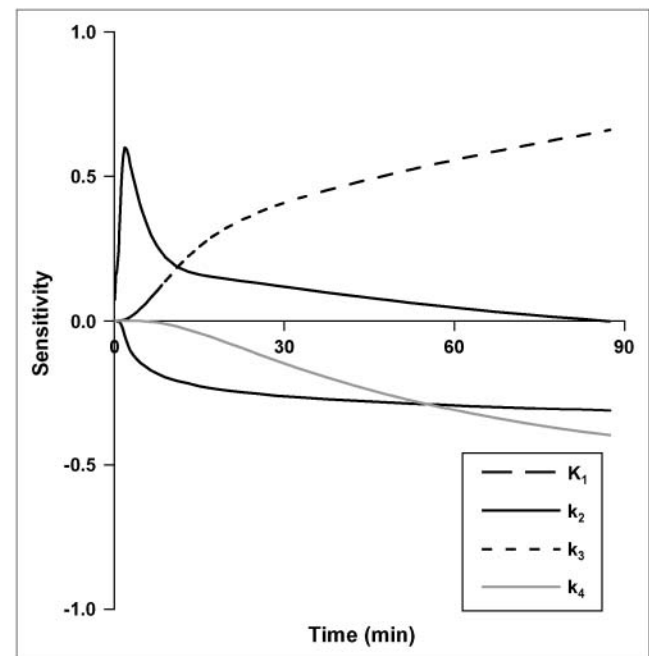


**FIGURE 2.** Sensitivity curves for brain parameters in FLT model. Sensitivity of each parameter is degree to which the model output is altered by 1% change in a model parameter.

**TABLE 3**  
Parameter Correlation Matrix for CE Tumors

Parameter	$K_1$	$K_1/k_2$	$k_3$	$k_4$
$K_1$	1	—	—	—
$K_1/k_2$	-0.68	1	—	—
$k_3$	0.56	<b>-0.97</b>	1	—
$k_4$	0.09	-0.63	0.38	1

Bold case indicates highly covariant parameters that were difficult to estimate independently.

C/L brain and CE glioma time–activity curves are summarized in Table 4. C/L brain and NCE tumors showed a similar level of variation. In the presence of statistical noise typical for  $^{18}\text{F}$ -FLT PET of gliomas ( $\sim 2\%$  time–activity curve coefficient of variation [COV] at 60 min), there was a SE of  $<10\%$  for the estimate of  $K_{\text{FLT}}$  and  $K_1$  for CE tumors. The other parameters ( $V_d$ ,  $k_3$ ,  $k_4$ ) had larger COV values and were less robust. The COV was greater in brain and NCE tumors ( $\sim 7\%$  time–activity curve COV at 60 min) than that in CE tumors, reflecting the low level of  $^{18}\text{F}$ -FLT transport and uptake in a nonproliferating tissue with restricted access at the BBB.

#### Model Accuracy

The accuracy of parameter estimates over a wide parameter range for brain is summarized in Table 5. The results of the simulation showed that the estimation of  $K_1$  is accurate over a wide clinical range using added noise typical of human CE tumor. The correlation coefficients for estimated versus true parameter values for  $K_1$  and  $K_{\text{FLT}}$  are 0.98 and 0.99, respectively, reflecting an accurate estimation process under the error conditions imposed. Correlation values were lower for  $k_3$  ( $r = 0.75$ ) and  $V_d$  ( $r = 0.76$ ), indicating less robust estimation as predicted by the sensitivity and identifiability analysis. The bias in the estimate was  $<2\%$  for  $K_1$  and for  $K_{\text{FLT}}$ . The precision of the estimates (SEE/mean) over the expected range was acceptable for  $K_{\text{FLT}}$  (4%) and  $K_1$  (12%) but was considerably poorer for  $V_d$ ,  $k_3$ , and  $k_4$ .

**TABLE 4**  
Errors in FLT Parameter Estimation Resulting from Introduction of Noise into Simulated Data\*

Location	$K_1$		$K_{\text{FLT}}$	
	Bias (%)	SE (%)	Bias (%)	SE (%)
CE glioma	1.2	7.0	3.1	6.1
C/L brain	24.2	48.8	-6.2	12.9

\*250 simulations for each tissue type with noise added typical of FLT CE glioma imaging (2% COV at 60 min).

**TABLE 5**  
Correlation Between Estimated and Actual Values for Simulated Data Generated Over Expected Clinical Range of Parameters\*

Parameter	$K_1$	$K_1/k_2$	$k_3$	$k_4$	$K_{\text{FLT}}$
$r$	0.98	0.76	0.75	0.60	0.99
Bias (%)	-1.9	-12.3	-8.9	1.9	-0.3
SEE/mean (%)	12.4	43.6	48.6	69.6	4.0

\*Expected clinical range for each parameter appears in Table 2.

#### Patient Imaging

Three examples of FLT patient image sets appear in Figure 3, including the coregistered MRI T1+Gd, FDG SUV, and FLT SUV from 30 to 60 min after injection, parametric images of transport and metabolic flux, as well as tissue time–activity curves. They demonstrate the anticipated variation in  $^{18}\text{F}$ -FLT uptake between tumor and brain with (Figs. 3A and 3C) and without (Fig. 3B) BBB breakdown. Nonproliferative, normal regions in the brain showed rapid early uptake and washout that mirrored the shape of the blood time–activity curve but was much lower in magnitude. In all cases, little retention was observed in normal brain. CE high-grade brain tumors (Fig. 3A) showed rapid early uptake with persistent retention. The  $^{18}\text{F}$ -FLT uptake pattern in NCE brain tumors was virtually identical to normal brain, presumably because of restricted access of  $^{18}\text{F}$ -FLT at the BBB.

#### Parameter Estimates

The mean and range of FLT model parameter estimates for CE and NCE tumors and gray and white matter are presented in Table 6. Model optimization results show that FLT is not retained to any significant degree in patients with an intact BBB or in C/L brain regions.  $K_1$  and  $K_{\text{FLT}}$  (Figs. 4A and 4B) were both significantly larger in CE ( $K_1$  mean, 0.053 mL/g/min,  $n = 9$ ;  $K_{\text{FLT}}$  mean, 0.018 mL/g/min,  $n = 9$ ) tumors than in NCE tumors (NCE  $K_1$  mean, 0.005 mL/g/min,  $n = 3$ ,  $P < 0.02$ ; NCE  $K_{\text{FLT}}$  mean, 0.001 mL/g/min,  $n = 3$ ,  $P < 0.005$ ). In CE tumors, which exhibited uptake and retention of  $^{18}\text{F}$ -FLT, the transport parameter  $K_1$  and  $K_{\text{FLT}}$  were closely correlated ( $r = 0.91$ ,  $n = 9$ ), suggesting that uptake of  $^{18}\text{F}$ -FLT is dominated by transport (Figs. 4C and 4D). Interestingly, 1 CE patient diagnosed with a previously treated low-grade oligodendroglioma with BBB breakdown (Fig. 3C) not only showed transport-dominated uptake ( $K_1 = 0.017$  mL/g/min) much larger than  $K_{\text{FLT}}$  (0.007 mL/g/min) but also had an estimated  $K_{\text{FLT}}$  value nearly as low as brain and much lower than high-grade gliomas. For comparison, TdR parameters reported previously for a similar set of glioma patients appear in Table 7 along with comparable FLT values.

The close correlation between  $K_1$  and  $K_{\text{FLT}}$  in patient studies prompted concern that the 2 might not be distinguishable over the range of parameters observed in glioma

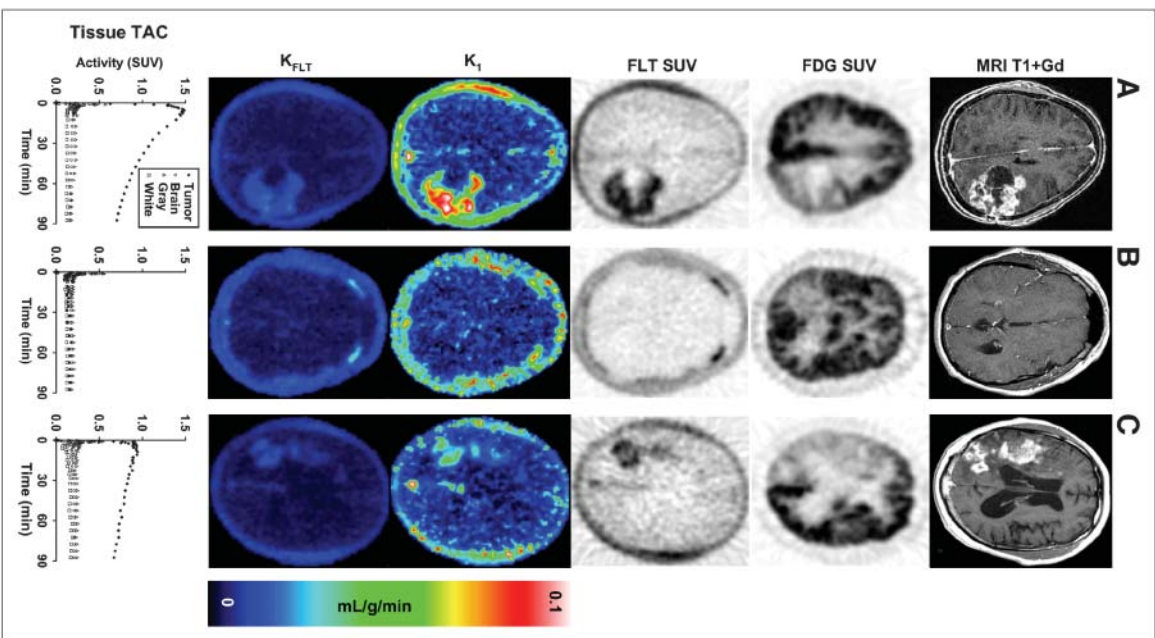


**FIGURE 3.** Three patients representing different aspects of FLT metabolism were investigated for <sup>18</sup>F-FLT uptake. (A) A 44-y-old woman with recurrent grade III anaplastic astrocytoma with BBB breakdown treated previously by radiotherapy (59 Gy). (B) A 56-y-old man with right parietal grade II oligodendroglioma with intact BBB treated previously by surgical resection followed by chemotherapy (procarbazine-lomustine-vincristine). (C) A 46-y-old man with recurrent grade II oligodendroglioma with BBB breakdown treated with radiotherapy (54 Gy) and chemotherapy (temozolomide) before PET. Surgery and therapy occurred at least 2 y before PET for all 3 patients. Coregistered images are as follows: MRI T1+Gd; FDG SUV summed 30–60 min; FLT SUV summed 30–60 min; parametric map of transport, K<sub>1</sub>; parametric image of metabolic flux, K<sub>FLT</sub>. TAC = time-activity curve.

patients. Therefore, we performed additional modeling simulations using the 2C model with various rates of initial transport (K<sub>1</sub> = 0.01, 0.025, and 0.050 mL/g/min), no phosphorylation (k<sub>3</sub> = 0) producing no flux, and added

**TABLE 6**  
Average FLT Model Parameters in Human Brain and Tumor Regions

Region	K <sub>1</sub> (mL/g/min)	K <sub>1</sub> /k <sub>2</sub> (1/min)	k <sub>3</sub> (1/min)	k <sub>4</sub> (1/min)	K <sub>FLT</sub> (mL/g/min)	K <sub>FLT-GA</sub> (mL/g/min)	MaxSUV
CE tumor ( <i>n</i> = 9)	0.053 (0.015, 0.126)	0.33 (0.18, 0.57)	0.093 (0.045, 0.129)	0.025 (0.017, 0.032)	0.018 (0.008, 0.033)	0.008 (0.005, 0.015)	2.22 (1.43, 3.26)
NCE tumor ( <i>n</i> = 3)	0.005 (0.003, 0.007)	0.24 (0.06, 0.43)	0.026 (0.002, 0.070)	0.018 (0.011, 0.033)	0.001 (0.001, 0.002)	0.001 (0.001, 0.002)	1.27 (0.11, 1.56)
High grade ( <i>n</i> = 9)	0.052 (0.005, 0.126)	0.30 (0.06, 0.57)	0.094 (0.045, 0.129)	0.024 (0.011, 0.032)	0.018 (0.002, 0.033)	0.007 (0.001, 0.015)	2.06 (1.16, 3.26)
Low grade ( <i>n</i> = 3)	0.008 (0.003, 0.015)	0.31 (0.23, 0.43)	0.021 (0.002, 0.055)	0.022 (0.011, 0.033)	0.003 (0.001, 0.008)	0.003 (0.001, 0.005)	1.73 (0.11, 2.5)
C/L brain ( <i>n</i> = 12)	0.004 (0.003, 0.006)	0.13 (0.06, 0.23)	0.045 (0.009, 0.118)	0.014 (0.003, 0.023)	0.002 (0.001, 0.003)	0.002 (0.001, 0.002)	1.30 (0.86, 2.11)
C/L gray matter	0.005 (0.003, 0.007)	0.16 (0.06, 0.33)	0.041 (0.002, 0.147)	0.019 (0.001, 0.061)	0.002 (0.001, 0.004)	0.002 (0.001, 0.002)	1.24 (0.81, 2.13)
C/L white matter	0.003 (0.002, 0.005)	0.14 (0.06, 0.26)	0.035 (0.008, 0.089)	0.011 (0.001, 0.024)	0.001 (0.001, 0.002)	0.001 (0.001, 0.002)	1.23 (0.82, 2.10)

$K_{FLT} = (K_1/k_3) \cdot (k_2 + k_3)$ ;  $K_{FLT-GA} = GA \text{ slope}$ .

Parentheses next to average contain minimum and maximum values.

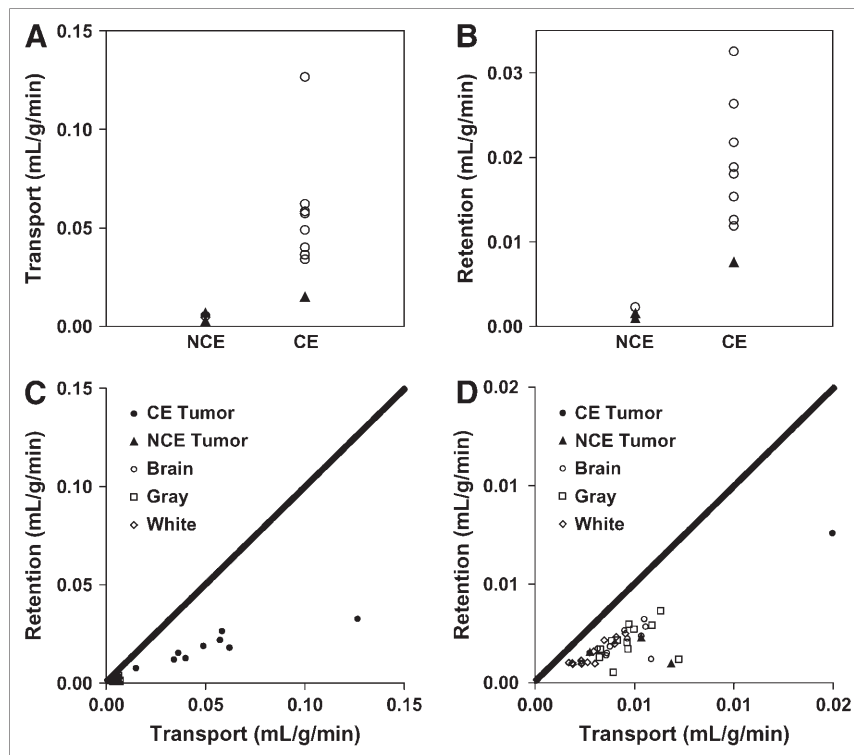


**FIGURE 4.** (A and B)  $^{18}\text{F}$ -FLT transport (A) and retention (B) parameter values plotted for NCE and CE glioma patients ( $n = 12$ ).  $\blacktriangle$ , Low-grade gliomas;  $\circ$ , high-grade tumors. (C) In plot of flux vs. transport parameter values ( $n = 12$ ), correlation is quite linear for tumor, but well under the line of identity, which may indicate effect of limited access of  $^{18}\text{F}$ -FLT to brain and tumor regions. (D) Same data as plotted in C with an expanded scale near the origin.

noise equivalent to 2% COV at 60 min on 200 datasets for each  $K_1$  level. Although flux was zero in the simulated curves ( $k_3 = 0$ ), when noise was added at a level typical of FLT brain imaging, the model-estimated average flux levels were 0.004, 0.008, and 0.011 mL/g/min for the range of  $K_1$  values used in the simulations. These flux values overlap with the range of flux values observed in the patient studies

for normal brain or low-grade gliomas and suggest that it will be difficult to estimate flux independent of transport at lower levels of metabolic flux.

$K_1$  is higher for MRI CE tumors than for NCE tumors ( $P < 0.02$ ) and  $K_{\text{FLT}}$  is higher in high-grade tumors (mean, 0.018;  $n = 9$ ) than that in lower-grade tumors (mean, 0.003;  $n = 3$ ,  $P < 0.01$ ). For CE tumors, we observed a finite rate

**TABLE 7**  
Comparison Between TdR Parameters Reported Previously and FLT in This Study

Tissue	Region	TdR				FLT				% $\Delta$
		Mean	Min	Max	$n$	Mean	Min	Max	$n$	
Transport ( $K_1$ )										
Tumor	NCE	0.018	0.005	0.028	13	0.005	0.003	0.007	3	-72
	CE	0.057	0.036	0.082	6	0.053	0.015	0.126	9	-7
	High	0.052	0.021	0.082	7	0.052	0.005	0.126	9	3
	Low	0.018	0.005	0.028	12	0.008	0.003	0.015	3	-8
C/L brain		0.020	0.007	0.051	24	0.004	0.003	0.006	12	-63
Metabolic flux ( $K_{\text{TdR}}$ or $K_{\text{FLT}}$ )										
Tumor	NCE	0.011	0.005	0.016	13	0.001	0.001	0.002	3	-88
	CE	0.041	0.019	0.059	6	0.018	0.008	0.033	9	-55
	High	0.030	0.016	0.059	7	0.018	0.002	0.033	9	-39
	Low	0.011	0.005	0.016	12	0.003	0.001	0.008	3	-49
C/L brain		0.011	0.001	0.022	24	0.002	0.001	0.003	12	-82
Mean flux ratio for FLT/TdR in C/L brain					0.23					
Mean flux ratio for FLT/TdR in high-grade gliomas					0.56					

NCE = noncontrast-enhancing tumor; CE = contrast-enhancing tumor with MRI T1+Gd imaging; High = glioma grades III and IV; Low = glioma grade II; %  $\Delta$  = percent difference in mean parameter value of TdR vs. FLT.

of late label loss, with an average estimate for  $k_4$  of  $0.025 \text{ min}^{-1}$  (range,  $0.017\text{--}0.032 \text{ min}^{-1}$ ;  $n = 9$ ). Consistent with this finding, a characteristic late downward curvature was observed in the GA plot for most CE gliomas. As previous reports have shown, ignoring  $k_4$  can lead to significant underestimation of flux (11,31).  $K_{\text{FLT}}$  values estimated from compartmental modeling analysis were correlated with GA  $K_{\text{FLT-GA}}$  ( $r = 0.84$ ) and FLT maximum SUV ( $r = 0.71$ ) and also highly correlated with  $K_1$  ( $r = 0.94$ ).

### Mixture Analysis

Mixture analysis–derived image maps of parameters were matched to ROI analysis for  $K_1$  ( $r = 0.98$ , SEE/mean = 5.9%,  $n = 10$ ) and  $K_{\text{FLT}}$  ( $r = 0.99$ , SEE/mean = 8.9%,  $n = 12$ ) (Fig. 5). Parametric images from the mixture analysis method did not reveal significant transport ( $K_1$ ) or flux ( $K_{\text{FLT}}$ ) outside of the regions of contrast enhancement. Examples of patient parametric images of transport and metabolic flux appear in Figure 3.

### DISCUSSION

$^{18}\text{F}$ -FLT PET may offer a noninvasive method for quantitating cellular proliferation in gliomas and may be useful for predicting disease progression and response to therapy. However, low tracer access to the brain and tumor tissue may limit the ability to infer proliferation from  $^{18}\text{F}$ -FLT retention. The purpose of the present study was to evaluate critically a compartmental model for quantitating  $^{18}\text{F}$ -FLT uptake and retention in glioma-bearing patients as an extension of previous modeling for somatic tumors (11). Kinetic analysis of  $^{18}\text{F}$ -FLT imaging was performed to estimate the extent to which  $^{18}\text{F}$ -FLT uptake was due to BBB breakdown versus tracer retention related to phosphorylation by TK1 and, therefore, tumor growth.

Our results indicate that accurate assessment of proliferation in brain by  $^{18}\text{F}$ -FLT imaging requires analysis of uptake kinetics to separate transport effects from tissue retention due to metabolic trapping of FLT nucleotides. This process involves an assay of the FLT fraction in blood, as blood clearance varied widely among the patients. It is

likely that the blood metabolite FLT-glucuronide does not enter normal cells (10) but may flow through the disrupted BBB into and out of the interstitial space during the imaging procedure. We assume the kinetics of this interaction and resulting tissue activity in normal and tumor regions can be accounted for by the vascular parameter  $V_b$ . Limited transit of FLT-glucuronide to and from the interstitial space is unlikely to affect model behavior, given the small quantity of the labeled metabolite present late in the imaging study.

As demonstrated in a patient with a recurrent pretreated low-grade oligodendroglioma with significant contrast enhancement (Fig. 3C), simple measures of tracer uptake, such as SUV, can be misleading when total  $^{18}\text{F}$ -FLT uptake is due in large part to transport across the BBB and not to trapping of FLT after phosphorylation by TK1. In addition, low transport can limit uptake even in proliferative tumors. Another patient (Table 1, patient. 2) with a grade III astrocytoma (determined by biopsy that showed 10% MIB-1 staining) had no contrast enhancement on MRI T1+Gd images.  $^{18}\text{F}$ -FLT uptake was similar to the low levels observed in normal brain. Simple measures of uptake that do not fully account for  $^{18}\text{F}$ -FLT transport, uptake, and loss from tissues can lead to incorrect interpretation of summed uptake images.

Transport impediments may pose a difficulty, however, in using FLT to assess residual viable brain tumor after therapy. In this case, transport may be transiently high because of treatment effects, and flux may be low in successfully treated tumors. The estimated  $K_{\text{FLT}}$  would then be mistakenly higher than the actual flux rate and could lead to a conclusion of residual tumor instead of successful treatment. One potential application of FLT may be for brain tumors with high initial  $K_1$  and  $K_{\text{FLT}}$ . After treatment, these patients may show an early reduction in  $K_{\text{FLT}}$  due to decreased proliferation. This hypothesis would need to be tested in serial  $^{18}\text{F}$ -FLT imaging studies over the course of therapy.

Compartmental modeling provides separate estimates of both transport and flux (trapping) to account for  $^{18}\text{F}$ -FLT uptake. Simulations suggest that the transport parameter can be estimated with <15% COV and metabolic flux with

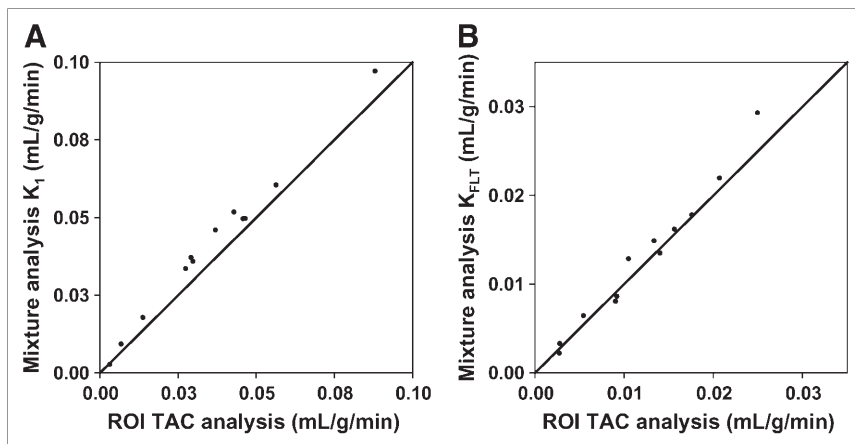


**FIGURE 5.** Parametric images generated by mixture analysis modeling results were highly correlated with conventional ROI modeling parameters for identical tissue regions for both transport (A) and retention (B). TAC = time–activity curve.

<5% COV. However, at the extremes of transport, modeling estimates of metabolic flux may be less accurate. For values of  $K_1$  close to that of normal brain and characteristic of NCE brain tumors, transport limits uptake and the flux cannot be measured independent of transport. Flux values for normal brain fall within the error of model estimates and reflect restricted access of FLT across the BBB. This also appears to be true for NCE or minimally CE brain tumors. Thus, FLT may be less useful in assessing proliferation in NCE tumors regardless of histopathology grading.

$^{18}\text{F}$ -FLT PET may also have difficulty in differentiating residual proliferating tumor from BBB breakdown in regions that are not highly proliferating. At the extreme of high  $K_1$  and low  $K_{\text{FLT}}$ , estimates of  $K_{\text{FLT}}$  are imprecise. In fact, simulations with high transport and no phosphorylation ( $k_3 = 0$ ) produced model estimates of flux that were non-zero. This may limit the applicability of FLT in circumstances of low flux, such as would be expected in radionecrosis. This is distinct from TdR imaging, where both flux and transport could be estimated over a wider range (21). The differences in model behavior result from differences in model transport ( $K_1$ ) and the retention or trapping ( $k_3$ ) rate, which are both higher for TdR than for the FLT analog.

We examined the relationship between  $^{18}\text{F}$ -FLT transport and metabolic flux using parametric image maps, which removes operator dependency in defining the ROI for kinetic analysis and allows visualization of the distribution of parameter values. Parametric image creation using mixture analysis produced regional maps of FLT kinetic parameters that were well correlated with time-activity curve parameter estimates of  $K_1$  and  $K_{\text{FLT}}$  (Fig. 5) and coincided with areas of CE on MRI T1+Gd images. As expected, patients without tumor enhancement on T1+Gd images showed uptake of FLT similar to the low levels observed in normal brain, which lends credence to the interpretation of  $K_1$  as transport across the BBB. Additionally, parametric image maps of overall flux and transport visually coincided with the extent of Gd contrast enhancement, suggesting the large influence of transport on FLT distribution in the brain.

We observed both qualitative and quantitative differences in results for FLT and TdR brain tumor imaging. For TdR, both flux and transport could be estimated over a wider range. The differences in model behavior for FLT versus TdR result from differences in the transport rate ( $K_1$ ) and the retention or trapping rate ( $k_3$ ), which are both higher for TdR than for FLT. FLT may not be transported by the same system as TdR. The saturable active nucleoside transport system for TdR at the BBB has significantly reduced transport for deoxynucleoside analogs with substitutions at the 3' position (24,25). Reports have suggested that the observed concentration gradient across the BBB after injection of  $^{18}\text{F}$ -FLT involves an active efflux transporter pumping FLT out from the brain (13). It is interesting to note that when this barrier has been disrupted as in CE gliomas, TdR and FLT have similar transport values (Table

7). The average metabolic flux of FLT in this study relative to the average flux of TdR reported previously (4) ( $K_{\text{FLT}}/K_{\text{TdR}}$ ; Table 7) for high-grade gliomas (0.56) and C/L brain (0.23) was in agreement with the TK1 phosphorylation ratio (PR) for FLT relative to TdR (PR = 0.3) (26,27). It was also comparable with the relative incorporation rate of FLT to TdR for cultured glioma cells in vitro (0.64) (32). These biologic factors underlie observed differences in transport and retention of these proliferation tracers.

One potential explanation for low transport and retention of  $^{18}\text{F}$ -FLT reported recently is competition with high levels of endogenous TdR, thus lowering the uptake of tracers such as FLT and TdR that use the exogenous pathway (33). Cellular assay studies on endogenous and exogenous TdR use reported that both pathways are used to a similar extent in tumor and normal cell lines (34), suggesting that reliance on the endogenous pathway does not restrict access to the exogenous pathway.

Low uptake of  $^{18}\text{F}$ -FLT could be due to predominant reliance on the de novo—versus the salvage—TdR pathways for incorporation into DNA. In a series of primary glioma and brain tissue specimens, Bardot et al. (35) observed a shift to the de novo pathway through a reduction in the ratio of TK to TdR synthase (TS) but that higher TK/TS ratios measured between normal brain and low-grade gliomas were statistically identical. This suggests that low  $^{18}\text{F}$ -FLT transport and retention in low-grade gliomas are not due to a predominant de novo synthesis of pyrimidines.

The simulation results show significant error in the estimation of the shape parameters ( $k_2$ ,  $k_3$ , and  $k_4$ ). A recent study on  $^{18}\text{F}$ -FLT in brain tumors (36) reported values of  $k_3$  for brain and gliomas, similar to ours, and concluded that the data do not support the hypothesis that estimation of glioma proliferation by  $^{18}\text{F}$ -FLT is accurate. Model simulations suggest that estimates of this parameter do not possess the precision required with small numbers of patients to evaluate this relationship. The model estimation error for  $k_3$  was approximately 50% for high-resolution simulations (2% COV at 60 min). Brain or NCE tumor tissue activity curves possess larger errors (7% COV at 60 min), which most likely would result in a much greater error in estimating  $k_3$ . Considering the variability in the estimation process, it is not surprising that  $k_3$  in tumor could not be differentiated from C/L brain.

An assessment of  $^{18}\text{F}$ -FLT uptake as an indicator of cell proliferation requires an independent measure of growth—for example, the determination of histopathologic proliferation markers such as Ki-67. A number of reports have found high correlations of Ki-67 with several measures of  $^{18}\text{F}$ -FLT uptake (reviewed by Mankoff et al. (2)). Individual rate parameters such as  $k_3$  are less robust than overall flux, which correlates to a modest degree (Spearman  $\rho = 0.70$ ,  $n = 12$ ) with pathologic grade. However, it is well known that the degree of BBB disruption tends to be higher in more proliferative tumors; therefore, this correlation may arise on the basis of transport.

## CONCLUSION

The use of  $^{18}\text{F}$ -FLT imaging to assess cellular proliferation in brain requires an analysis of dynamic FLT metabolism to separate transport effects from tissue retention of metabolically trapped FLT nucleotides. With compartmental modeling techniques, the FLT flux in CE brain tumors can be measured with a SE of  $<5\%$  and  $^{18}\text{F}$ -FLT transport can be estimated with a SE of  $<15\%$ .

Normal brain and NCE tumors with an intact BBB have very limited transport and cannot be adequately assessed for cellular proliferation by  $^{18}\text{F}$ -FLT. In addition, problems interpreting images are encountered for patients with high  $K_1$  and low  $K_{\text{FLT}}$ , as might be encountered in radionecrosis.  $^{18}\text{F}$ -FLT may not be useful for NCE gliomas regardless of histopathologic grading or proliferation state.  $^{18}\text{F}$ -FLT PET may also have difficulty in differentiating residual proliferating brain tumor from BBB breakdown in regions that are not highly proliferating.  $^{18}\text{F}$ -FLT brain imaging might have potential use in managing gliomas with initially high  $K_1$  and high  $K_{\text{FLT}}$  for evaluation of early response to new therapies. In that case, it is likely that an early posttreatment decline in  $K_{\text{FLT}}$  would be observed before a change in  $K_1$ .

## ACKNOWLEDGMENTS

We greatly appreciate the assistance of Pam Pham for assistance in all patient imaging and reconstruction procedures. This work is supported by National Cancer Institute grants CA42045 and S10 RR17229.

## REFERENCES

1. Eary JF, Mankoff DA, Spence AM, et al. 2-[C-11]Thymidine imaging of malignant brain tumors. *Cancer Res.* 1999;59:615–621.
2. Mankoff DA, Shields AF, Krohn KA. PET imaging of cellular proliferation. *Radiol Clin North Am.* 2005;43:153–167.
3. Shields AF, Mankoff DA, Link JM, et al. Carbon-11-thymidine and FDG to measure therapy response. *J Nucl Med.* 1998;39:1757–1762.
4. Wells JM, Mankoff DA, Eary JF, et al. Kinetic analysis of 2-[ $^{11}\text{C}$ ]thymidine PET imaging studies of malignant brain tumors: preliminary patient results. *Mol Imaging.* 2002;1:145–150.
5. Shields AF, Grierson JR, Kozawa SM, Zheng M. Development of labeled thymidine analogs for imaging tumor proliferation. *Nucl Med Biol.* 1996;23:17–22.
6. Mankoff DA, Shields AF, Graham MM, Link JM, Eary JF, Krohn KA. Kinetic analysis of 2-[carbon-11]thymidine PET imaging studies: compartmental model and mathematical analysis. *J Nucl Med.* 1998;39:1043–1055.
7. Cornford EM, Oldendorf WH. Independent blood-brain barrier transport systems for nucleic acid precursors. *Biochim Biophys Acta.* 1975;394:211–219.
8. Grierson JR, Shields AF. Radiosynthesis of 3'-deoxy-3'-[ $^{18}\text{F}$ ]fluorothymidine: [ $^{18}\text{F}$ ]FLT for imaging of cellular proliferation in vivo. *Nucl Med Biol.* 2000;27:143–156.
9. Grierson JR, Schwartz JL, Muzi M, Jordan R, Krohn KA. Metabolism of 3'-deoxy-3'-[F-18]fluorothymidine in proliferating A549 cells: validations for positron emission tomography. *Nucl Med Biol.* 2004;31:829–837.
10. Kong XB, Zhu QY, Vidal PM, et al. Comparisons of anti-human immunodeficiency virus activities, cellular transport, and plasma and intracellular pharmacokinetics of 3'-fluoro-3'-deoxythymidine and 3'-azido-3'-deoxythymidine. *Antimicrob Agents Chemother.* 1992;36:808–818.
11. Muzi M, Vesselle H, Grierson JR, et al. Kinetic analysis of 3'-deoxy-3'-fluorothymidine PET studies: validation studies in patients with lung cancer. *J Nucl Med.* 2005;46:274–282.
12. Muzi M, Mankoff DA, Grierson JR, Wells JM, Vesselle H, Krohn KA. Kinetic modeling of 3'-deoxy-3'-fluorothymidine in somatic tumors: mathematical studies. *J Nucl Med.* 2005;46:371–380.
13. Stahle L, Borg N. Transport of alovudine (3'-fluorothymidine) into the brain and the cerebrospinal fluid of the rat, studied by microdialysis. *Life Sci.* 2000;66:1805–1816.
14. Curnes JT, Laster DW, Ball MR, Moody DM, Witcofski RL. MRI of radiation injury to the brain. *AJR.* 1986;147:119–124.
15. Blocher A, Bieg C, Ehrlichmann W, Dohmen BM, Machulla HJ. Procedures for the routine synthesis of [ $^{18}\text{F}$ ]FLT in high activities [abstract]. *J Nucl Med.* 2001;42(suppl):257P.
16. Lewellen TK, Kohlmyer SG, Miyaoka RS, Kaplan MS, Stearns CW, Schubert SF. Investigation of the performance of the General Electric ADVANCE positron emission tomograph in 3D mode. *IEEE Trans Nucl Sci.* 1996;43:2199–2206.
17. Graham MM, Lewellen BL. High-speed automated discrete blood sampling for positron emission tomography. *J Nucl Med.* 1993;34:1357–1360.
18. Kinahan PE, Townsend DW, Beyer T, Sashin D. Attenuation correction for a combined 3D PET/CT scanner. *Med Phys.* 1998;25:2046–2053.
19. Lundgren B, Bottiger D, Ljungdahl-Stahle E, et al. Antiviral effects of 3'-fluorothymidine and 3'-azidothymidine in cynomolgus monkeys infected with simian immunodeficiency virus. *J Acquir Immune Defic Syndr.* 1991;4:489–498.
20. Vesselle H, Grierson J, Muzi M, et al. In vivo validation of 3'-deoxy-3'-[ $^{18}\text{F}$ ]fluorothymidine ([ $^{18}\text{F}$ ]FLT) as a proliferation imaging tracer in humans: correlation of [ $^{18}\text{F}$ ]FLT uptake by positron emission tomography with Ki-67 immunohistochemistry and flow cytometry in human lung tumors. *Clin Cancer Res.* 2002;8:3315–3323.
21. Wells JM, Mankoff DA, Muzi M, et al. Kinetic analysis of 2-[ $^{11}\text{C}$ ]thymidine PET imaging studies of malignant brain tumors: compartmental model investigation and mathematical analysis. *Mol Imaging.* 2002;1:151–159.
22. Chishty M, Begley DJ, Abbott NJ, Reichel A. Functional characterisation of nucleoside transport in rat brain endothelial cells. *Neuroreport.* 2003;14:1087–1090.
23. Phelps ME, Huang SC, Hoffman EJ, Selin C, Sokoloff L, Kuhl DE. Tomographic measurement of local cerebral glucose metabolic rate in humans with [F-18]2-fluoro-2-deoxy-D-glucose: validation of method. *Ann Neurol.* 1979;6:371–388.
24. Gati WP, Misra HK, Knaus EE, Wiebe LJ. Structural modifications at the 2'- and 3'-positions of some pyrimidine nucleosides as determinants of their interaction with the mouse erythrocyte nucleoside transporter. *Biochem Pharmacol.* 1984;33:3325–3331.
25. Spector R, Huntoon S. Specificity and sodium dependence of the active nucleoside transport system in choroid plexus. *J Neurochem.* 1984;42:1048–1052.
26. Eriksson S, Kierdaszuk B, Munch-Petersen B, Oberg B, Johansson NG. Comparison of the substrate specificities of human thymidine kinase 1 and 2 and deoxycytidine kinase toward antiviral and cytostatic nucleoside analogs. *Biochem Biophys Res Commun.* 1991;176:586–592.
27. Arner ES, Spasokoukotskaja T, Eriksson S. Selective assays for thymidine kinase 1 and 2 and deoxycytidine kinase and their activities in extracts from human cells and tissues. *Biochem Biophys Res Commun.* 1992;188:712–718.
28. O'Sullivan F. Metabolic images from dynamic positron emission tomography studies. *Stat Methods Med Res.* 1994;3:87–101.
29. O'Sullivan F. Imaging radiotracer model parameters in PET: a mixture analysis approach. *IEEE Trans Med Imaging.* 1993;12:399–412.
30. Mankoff DA, Shields AF, Graham MM, Link JM, Krohn KA. A graphical analysis method to estimate blood-to-tissue transfer constants for tracers with labeled metabolites. *J Nucl Med.* 1996;37:2049–2057.
31. Patlak CS, Blasberg RG. Graphical evaluation of blood-to-brain transfer constants from multiple-time uptake data: generalizations. *J Cereb Blood Flow Metab.* 1985;5:584–590.
32. Toyohara J, Waki A, Takamatsu S, Yonekura Y, Magata Y, Fujibayashi Y. Basis of FLT as a cell proliferation marker: comparative uptake studies with [ $^3\text{H}$ ]thymidine and [ $^3\text{H}$ ]arabinothymidine, and cell-analysis in 22 asynchronously growing tumor cell lines. *Nucl Med Biol.* 2002;29:281–287.
33. Tseng JR, Dandekar M, Subbarayan M, et al. Reproducibility of 3'-deoxy-3'-[ $^{18}\text{F}$ ]fluorothymidine microPET studies in tumor xenografts in mice. *J Nucl Med.* 2005;46:1851–1857.
34. Shields AF, Coonrod DV, Quackenbush RC, Crowley JJ. Cellular sources of thymidine nucleotides: studies for PET. *J Nucl Med.* 1987;28:1435–1440.
35. Bardot V, Dutrillaux AM, Beaumatin J, et al. Purine and pyrimidine metabolisms in human gliomas, melanomas and colon carcinomas xenografts: relation to their cytogenetic profile. *Adv Exp Med Biol.* 1994;370:219–225.
36. Jacobs AH, Thomas A, Kracht LW, et al.  $^{18}\text{F}$ -Fluoro-L-thymidine and  $^{11}\text{C}$ -methylmethionine as markers of increased transport and proliferation in brain tumors. *J Nucl Med.* 2005;46:1948–1958.